Journal of Materials Chemistry A

Accepted Manuscript

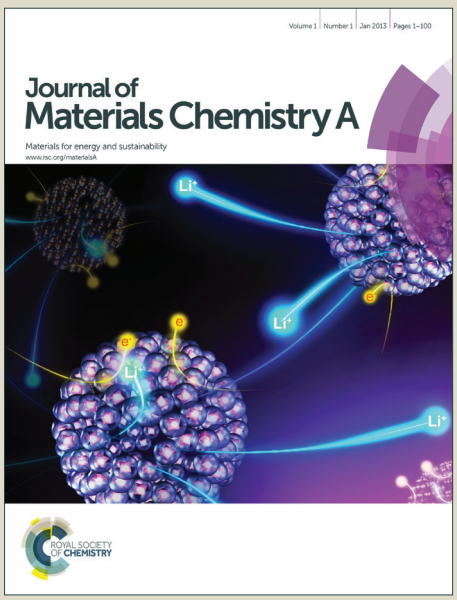

ROYAL SOCIETY OF CHEMISTRY

www.rsc.org/materialsA

Journal of Materials Chemistry A

Dynamic Article Links ►

Cite this: DOI: 10.1039/c0xx00000x

www.rsc.org/xxxxxx

PAPER

Optimizing the Charge Transfer Process by Design of Co_3O_4@PPy@MnO_2 Ternary Core-Shell Composite

Bin Wang,[a] Xinyi He,[a] Hongpeng Li,[a] Qi Liu,[a] Jun Wang,*[ac] Lei Yu,[a] Huijun Yan,[a] Zhanshuang Li[a] and Peng Wang[b]

Received (in XXX, XXX) Xth XXXXXXXXX 20XX, Accepted Xth XXXXXXXXX 20XX

DOI: 10.1039/b000000x

In this paper, the incorporation of high conductive material (Polypyrrole) into binary metal oxide core-shell structured composite is adopted to optimize the charge transfer process to further improve electrochemical performance. Due to enhanced electron transfer ability, charge transfer resistances of the ternary core-shell structured composites are all reduced and the electrochemical performances are also improved. For example, the Co_3O_4@PPy@MnO_2 ternary core-shell heterostructured composite exhibits high specific capacitance and excellent rate capability (53% of capacity retention rate at 40 A/g compared with 782 F/g at 0.5 A/g). The composite shows good cycling stability with 97.6% capacity retention over 2000 cycles at 5 A/g. These results demonstrate the potential of core-shell composites to further improve high performance in supercapacitor electrodes.

1. Introduction

The rapid increase of demand for renewable energy has driven the development of electrochemical energy storage (EES) devices. Electrochemical capacitors (ECs), also known as supercapacitors, are considered one of the key technology systems which have a wide range of application due to their high power density, long cycling lifestyle and environmental-friendliness [1,2]. With respect to the core of ECs, the electrode materials can be divided into three groups: (i) carbon materials [3,4] (ii) conducting polymers [5,6] and (iii) metal oxides [7-10]. Apart from high specific surface area, the design of nanoarchitectures for EC electrodes is an effective way to improve electrochemical performance. This is because the nanoarchitecture gives a broader real reaction area and enhances the efficient charge and mass exchange [11,12]. Three-dimensional (3D) nanostructured materials, such as 3D carbon materials [13-15] and the advanced core-shell heterostructure materials [16-19], have attracted most of the researchers' attention in recent years because of their superior performance [20,21].

Core-shell nanostructured material, is a hybrid material, comprising various types of materials in arbitrary combination, such as metal oxide/metal oxide [22-24], metal oxide/metal hydroxide [25-27], metal oxide/conductive polymer [28,29], and carbon materials/metal oxide [30-33]. The testing results show that the synergistic effect caused by the structure has an advantageous effect on electrochemical performance. The charge transfer resistance (R_{ct}) of the hybrid core/shell materials is relatively high, especially for MnO_2 based core/shell materials, as shown in Table S1. The highest R_{ct} is 155 Ω (Aligned Carbon Nanofiber Arrays@MnO_2) and even the more improved values are between 3-5 Ω. Other metal oxide based core materials also show a higher R_{ct}. Electrochemical performance is closely linked with the charge transfer resistance, so a reduction in R_{ct} results is a significant improvement in electrochemical performance. Optimizing the core material becomes a feasible option. Lee and his group choose ITO nanowires as core; their contrastive electrochemical results demonstrate that higher conductivity core material improves the charge transfer process [10,34,35]. Moreover, a porous core material also accomplishes this effect [36]. Therefore, the purpose of this article is to find an effective way to further reduce the charge transfer resistance.

The unique hierarchical core-shell and heterostructured configuration, along with the synergistic effects of the combined materials, clearly promote charge transfer process [8,9,16,30,32,37]. This indicates that the structure has the potential to be further investigated. In the present work, our main approach is to incorporate higher conductive material into the binary core-shell structure to solve the problem of high charge

transfer resistance. Through the layer-by-layer process, the ternary core-shell nanostructure is fabricated. As proof, Co_3O_4@PPy@MnO_2 ternary core-shell composite is described in detail. Compared with the binary core-shell composite, the electrochemical analysis results show that the charge transfer process of Co_3O_4@PPy@MnO_2 ternary core-shell composite is improved: the value of R_{ct} declines significantly (0.94 Ω, compared with Co_3O_4@PPy: 12.87 Ω and Co_3O_4@MnO_2: 60.9 Ω). And it's easy to understand that the electrochemical performance of Co_3O_4@PPy@MnO_2 is better than either Co_3O_4@PPy or Co_3O_4@MnO_2: the specific capacitance is 2~3 times higher than the binary core-shell composite (782 F/g, 265 F/g and 306 F/g respectively). In addition, we analyze the electrochemical behavior of other ternary core-shell composites: Co_3O_4@PPy@NiOOH, Co_3O_4@PANI@MnO_2 and Co_3O_4@PANI(polyaniline)@NiOOH. Compared with binary core-shell structured composites, the R_{ct} of ternary core-shell structured composites all decline significantly, showing that the charge transfer process is optimized. These results indicate that incorporation of high conductive material is an effective way to improve the electrochemical performance of binary core-shell structured composites.

2. Results and Discussion

The ternary core-shell Co_3O_4@PPy@MnO_2 was synthesized by a layer-by-layer process: First, Co_3O_4 nanowires were grown onto the Cu foil vertically by a hydrothermal method, followed by calcination. Secondly, a PPy layer was coated onto Co_3O_4 nanowires via monomer polymerization. Finally, MnO_2 nanoparticles were onto Co_3O_4@PPy through the reaction of MnO^{4-} and Mn^{2+}. While the $KMnO_4$ solution reacts with the conductive polymer and carbon materials. In order to get the maximize protection of the conductive polymer layer, the Co_3O_4@PPy composite was soaked in Mn^{2+} solution completely. In addition, we reduced the concentration of $KMnO_4$ solution and the reaction time (details seen in methods in ESI). Finally, we repeated the operation to increase the quality of MnO_2. The contrastive scanning electron microscopy (SEM) images of the prepared binary core-shell composites and the ternary core-shell composite are shown in Figure 1. After the coating process, all core-shell composites remain as nanowire-structures (seen in Figure S1 A-D in ESI), while the density of the composites changes: the interspace among ternary core-shell composite is the smallest (Figure S1 D in ESI); the binary core-shell composites are larger (Figure S1 B,C in ESI); and the pure Co_3O_4 nanowires are

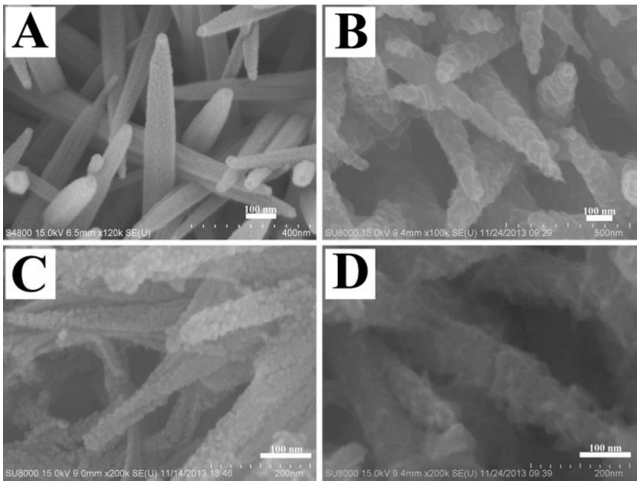

Figure 1. SEM images of Co_3O_4 nanowire (A), Co3O4@PPy (B), Co_3O_4@MnO_2 (C) binary core-shell composites and Co_3O_4@PPy@MnO_2 (D) ternary core-shell composite.

the largest. This core-shell composite formation demonstrates a successful layer-by-layer coated process. In addition, Figure 1 gives an obvious surface morphology change of the four composites. Compared with the pure Co_3O_4 nanowire(Figure 1A); the Co_3O_4@PPy nanowire shows several embossment after coating PPy layer (Figure 1B), and more nanoparticle is growth on the surface of Co_3O_4 nanowire (Figure 1C). Figure 1D shows the SEM image of Co_3O_4@PPy@MnO_2 nanowire. Compared with the Co_3O_4@PPy nanowire, a layer of MnO_2 nanosheets is grown after the reaction of MnO^{4-} and Mn^{2+}. The compared result indicates a successful layer-by-layer growth process.

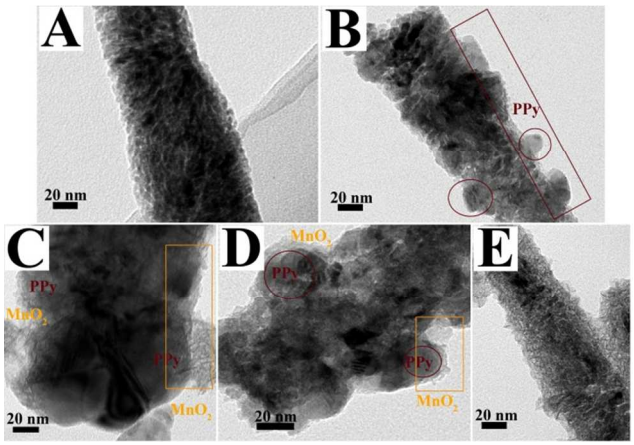

Figure 2. TEM images of Co_3O_4 nanowire (A), Co_3O_4@PPy (B) and Co_3O_4@PPy@MnO_2 (C-E).

Figure 2 shows the transmission electron microscopy (TEM) images of the prepared core-shell nanostructured composites. Compared with the single Co_3O_4 nanowires (Figure 2A), all of the core-shell composites reflect a typical hierarchical structure (seen in Figure 2B for Co_3O_4@PPy and Figure S2 A in ESI for Co_3O_4@MnO_2). As shown in Figure 2B, the PPy layer is covered onto the Co_3O_4 nanowires, the embossment is also appeared, which is consist with Figure 1B. Figure 2C-D gives the structure

of Co_3O_4@PPy@MnO_2 ternary core-shell composite with one repeat number of growing MnO_2. PPy is coated onto Co_3O_4 nanowires and a small amount of MnO_2 is coated onto the PPy layer. This is more obvious on the embossment part in Figure 2D. When the repeat number is increased, the incorporated PPy layer is covered with MnO_2 nanosheets (Figure 2E), and this is consist with the SEM image in Figure 1D. Because the incorporated PPy layer also reacts with $KMnO_4$, the outer layer is composed of MnO_2 nanosheets (compared with the Co_3O_4@MnO_2). In addition, the repeat number also plays a role. Moreover, the diverging nanosheet structure supplies a broader contact area with the electrolyte. This is one of the reasons why the electrochemical performance of Co_3O_4@PPy@MnO_2 is better than Co_3O_4@MnO_2.

The X-ray diffraction (XRD) pattern of Co_3O_4@PPy@MnO_2 composite shows the characteristic peaks of Co_3O_4 (at 2θ=38.1°) and MnO_2 (at 2θ=12.5°, 25.6° and 36.2°) (Figure 3A) [15,38]. The Fourier transform infrared spectroscopy (FTIR) image in Figure 3B shows the existence of the PPy layer. The bands at 1579 and 1440 cm^{-1} are attributed to the antisymmetric and symmetric vibrations of the pyrrole ring. Bands at 1156 and 850 cm^{-1} correspond to δ-CH. All of these confirm the presence of PPy. In addition, the characteristic peaks appear at about 663, 530 cm^{-1} belong to Co-O in CO_3O_4 and the peak at 425 cm^{-1} is indicative of vibrations Mn-O in MnO_2, indicating the existence of Co_3O_4 and MnO_2. These results are consistent with the literatures. [29,39,40]. A comparison with the energy-dispersive X-ray spectrometry (EDS) mapping analysis achieves the same result as FTTR (Figure S3 and S4 in ESI). The X-ray photoelectron spectroscopy (XPS) patterns is used to further analyze the Co_3O_4@PPy@MnO_2 composite. As shown in N 1s XPS pattern in Figure 3D, the two pronounced peak centers at 399.4 eV (-NH-) and 397.6 eV (=N-) testify the existence of PPy layer. [41-43] In addition, the Co 2p (Figure 3C) and the Mn 2p (Figure 3E) XPS patterns confirm the cobalt existing in the form of Co_3O_4 and the manganese existing in the form of MnO_2. [15,42] The above analysis certify the successful preparation of Co_3O_4@PPy@MnO_2 composite

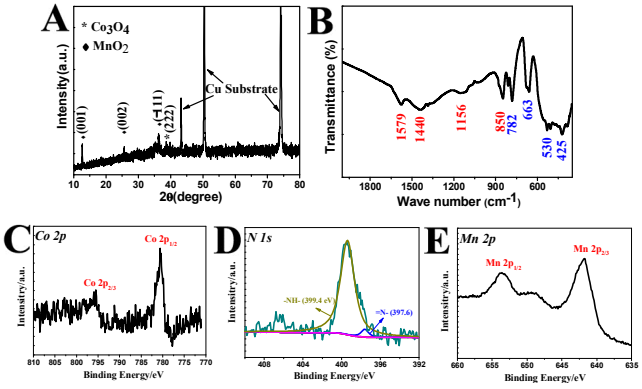

Figure 3. XRD (A), FTIR (B) patterns of Co_3O_4@PPy@MnO_2 composite, Co 2p (C) N 1s (D) and Mn 2p (E) XPS patterns of Co_3O_4@PPy@MnO_2 composite.

The electrochemical performance of the core-shell composites is tested in 1 M KOH aqueous solution with the three-electrode system. Figure 4A and 4B give a comparison of the cyclic voltammetry (CV) curves and galvanostatic charge/discharge (CD) curves of the pure Co_3O_4, binary core-shell composites (Co_3O_4@PPy and Co_3O_4@MnO_2), and the ternary core-shell composite (Co_3O_4@PPy@MnO_2). The repeat number of growing MnO_2 onto Co_3O_4 nanowires and Co_3O_4@PPy nanowires is four. All CV curves reflect pseudocapacitive behavior: the asymmetrical shape and the redox peaks. The CV curves exhibit one anodic peak (0.5V) and two cathodic peaks (0.428V and 0.366V), which correspond to Co^{2+}/Co^{3+} (Eq.1) and Co^{3+}/Co^{4+} (Eq.2) [44].

$$CoOOH + OH^- \Leftrightarrow CoO_2 + H_2O + e^- \quad (1)$$

$$Co_3O_4 + H_2O + OH^- \Leftrightarrow 3CoOOH + e^- \quad (2)$$

Compared with pure Co_3O_4, the CV curves of the binary core-shell composites are expanded, indicating much better electrochemical performance due to the hierarchical heterostructure. Among the core-shell composites, the current response of the Co_3O_4@PPy@MnO_2 composite is the highest, indicating the best electrochemical performance. In addition, the CV curve of the Co_3O_4@PPy@MnO_2 composite is roughly rectangular in shape (Figure 4C) when excluding the effect of Co_3O_4, this is due to the pseudocapacitance mechanisms of MnO_2 (Eqs.3 and 4) in KOH solution [45].

$$(MnO_2)_{surface} + K^+ \Leftrightarrow (MnO_2^- K^+)_{surface} \quad (3)$$

$$(MnO_2)_{bulk} + K^+ + e^- \Leftrightarrow (MnOOK)_{bulk} \quad (4)$$

Reaction (3) is related to the real contact area of MnO_2 with the electrolyte solution, and a more convenient ion diffusion pathway also has a reactive role (associated with the structure). In this work, the unique hierarchical core-shell heterostructure not only has a high specific surface area but also facilitates electrolyte penetration, while the key to reaction (4) is whether electrons can transfer inside the composite effectively.

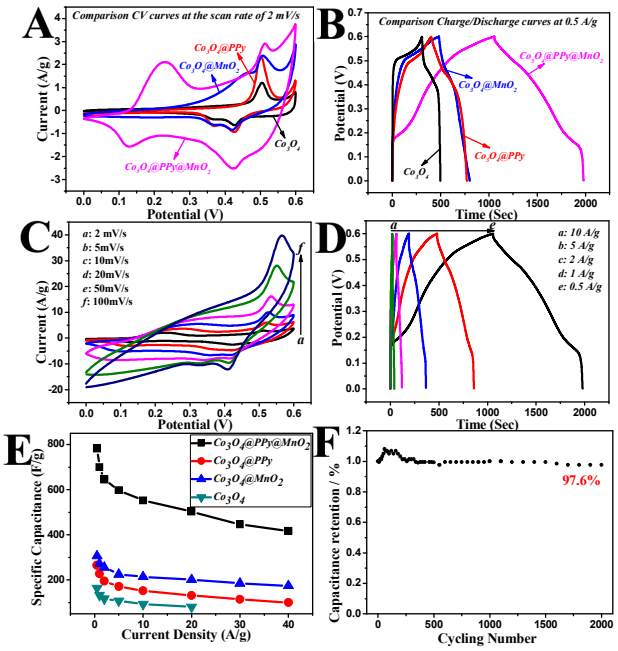

Figure 4. Compared CV curves (A) and CD curves (B) for pure Co_3O_4, Co_3O_4@PPy, Co_3O_4@MnO_2 and Co_3O_4@PPy@MnO_2. (C) The CV curves for Co_3O_4@PPy@MnO_2 at various scan rates. (D) CD curves of Co_3O_4@PPy@MnO_2 at various current densities. (E) Compared specific capacitances. (F) Cycling performance of Co_3O_4@PPy@MnO_2.

Figure 4B gives the comparison of CD curves at 0.5 A/g. The CD curve of the pure Co_3O_4 electrode can be divided into two parts: 1) electric double layer capacitance behavior starts from 0 to 0.48 V; during this section the capacitance is caused by the charge adsorption on the interface. 2) the Faraday process at high potential, and the capacitance is due to the redox reaction. The specific capacitance of Co_3O_4 electrode is 164 F/g at 0.5 A/g (Figure 4E). The CD curves of the binary core-shell composites are similar to the CD of Co_3O_4. Although the electrochemical performance is improved (265 and 306 F/g at 0.5 A/g for Co_3O_4@MnO_2 and Co_3O_4@PPy respectively), the result is not ideal. This is due to the high charge transfer resistance for binary core-shell composites (Table S7 in ESI). The CD curve of the Co_3O_4@PPy@MnO_2 composite is similar to a triangular shape, which is caused by the coated MnO_2 nanosheets [14,30]. Compared with Co_3O_4@MnO_2, the specific capacitance of the Co_3O_4@PPy@MnO_2 ternary core-shell composite is 782 F/g. The reasons are as follows: the intermediary PPy layer gives a larger effective reaction area with high conductivity for MnO2, and reaction (4) of Co_3O_4@PPy@MnO_2 composite is more powerful. Because of the lower conductivity of the Co_3O_4 nanowires and a smaller effective reaction area, the electrochemical performance of MnO_2 on Co_3O_4@MnO_2 composite is not fully reflected. The shape of the two CD curves are the following: for Co_3O_4@MnO_2 composite, the redox of Co_3O_4 occupies the leading position, the CD curve is similar to the pure Co_3O_4, only the charge and discharge time is enlarged. For Co_3O_4@PPy@MnO_2 composite, the redox of MnO_2 occupies the leading position, the charging and discharging platform of Co_3O_4 is buffered. This is consistent with the compared CV curves in Figure 4A.

Figure 4C gives the CV curves of Co_3O_4@PPy@MnO_2 composite at various scan rates. The redox peaks of Co_3O_4 move towards both sides with increasing scan rate (Figure 4C). The result is consistent with other composites (shown in Figure S5 A-C in ESI). The roughly rectangular shape caused by MnO_2 is maintained at high scan rates. The CD series curves are shown in Figure 4D. All CD curves maintain the triangular shape, and the specific capacitance calculated based on the discharging curves decreases with the increase of current density (Figure 4E). This is because the electrochemical reaction of the electrode is effected by the material itself, the ionic diffusion near the electrode interface, and the electronic transmission inside the electrode. With regard to the latter two mutual constraints, a high electronic transmission rate does not mean high specific capacitance if the supply of reaction ions from the solution are not adequate to the meet the demand of the redox reaction. Thus the polarization phenomenon is more obvious at high current densities and the IR drop increases. For example, at 0.5 A/g, the IR drop for Co_3O_4@PPy@MnO_2 is only 0.01V, while the value is 0.1V at 10 A/g. The proportion increases from 1.7% to 17% compared with the whole potential windows. Still, the specific capacitance of Co_3O_4@PPy@MnO_2 composite is 53% at 40 A/g (417 F/g, compared with 782 F/g at 0.5 A/g). The rate capabilities of Co_3O_4@PPy and Co_3O_4@MnO_2 are 58% (306 F/g at 0.5 A/g and 174 F/g at 40 A/g) and 38% (265 F/g at 0.5 A/g and 100 F/g at 40 A/g). A comparison of the data indicates that the intermediary PPy layer improves the rate capability of ternary core-shell structured composite. Specific area capacitance is another crucial factor for the supercapacitor electrode. The average loading masses of the four composites are 0.2 mg/cm^2 (pure Co_3O_4), 0.35 mg/cm^2 (Co_3O_4@MnO_2), 0.5 mg/cm^2 (Co_3O_4@PPy) and 0.7 mg/cm^2 (Co_3O_4@PPy@MnO_2). The specific area capacitances of Co_3O_4@PPy@MnO_2 composite at 0.5, 1, 2, 5, 10 A/g are 0.55, 0.49, 0.45, 0.42 and 0.38 F/cm^2; even at 40 A/g, the value is 0.29 F/cm^2 (Figure S6 in ESI). The value is 3~6 times higher than binary core-shell structured composites (0.093 and 0.153 F/cm^2 at 0.5 A/g for Co_3O_4@MnO_2 and Co_3O_4@PPy). Furthermore, this value is much higher than MnO_2 coated core-shell composites, such as hydrogenated single-crystal ZnO@amorphous ZnO-doped MnO_2 core-shell nanocables (138.7 mF/cm^2 at 1 mA/cm^2) [46], WO_{3-x}@Au@MnO_2 core-shell nanowires onto carbon fabric (105 mF/cm^2 at 0.06 mA/cm^2) [23], NiO@MnO_2 nanoflakes (0.4 F/cm^2 at 5 mA/cm^2) [16], hydrogenated TiO_2@MnO_2 nanowires (70 mF/cm^2 at 2 mA/cm^2) [47], and so on [48-50]. Figure 4F gives the cycling performance of Co_3O_4@PPy@MnO_2 composite at the current density of 5 A/g. At first the composite is actives and the performance is fluctuating and becomes stable at about 250th cycling. Finally the specific capacitance remains 97.6% after 2000th cycling, showing a fairly good stability.

Remarkably, the electrochemical performance of Co_3O_4@PPy@MnO_2 ternary core-shell composite is better than Co_3O_4@MnO_2 and Co_3O_4@PPy. As we mentioned above, the incorporated higher conductivity PPy layer optimizes the charge transfer process, so the reduction of charge transfer resistance will provide the most intuitive performance. A further study of electrochemical impedance spectroscopy (EIS) is shown in Figure 5. The EIS patterns in Figure 5B reflect a hybrid control process: 1) charge transfer controlled at high frequency, showing

the semicircle in EIS. The shape in our test deviates from the standard semicircle, due to the heterogeneity of the electrode/solution interface (such as the electrode surface roughness, different electrochemical activity and uneven electric field) and can be expressed as the constant phase angle part (Z_{CPE}). The charge transfer resistance (R_{ct}) and the equivalent series resistance (R_s, including the active material, the current collector and the electrolyte) can be obtained by the diameter of the semicircle and the intercept of the X axis. 2) The diffusion, controlled at low frequency, shows a straight line with the slope close to infinity. This is caused by the adsorption of ions onto the electrode surface (reactions 1-4 need the participation of ions from the solution). The equivalent circuit diagram is shown in Figure 5A: *Zw* is the Warburg resistance (composed of the diffusion resistance and the diffusion capacitance) and C_L is the capacitance limit. The R_{ct} of Co_3O_4@PPy@MnO_2 is 0.94 Ω, the value is much smaller than Co_3O_4@MnO_2 (60.9 Ω) and Co_3O_4@PPy (12.87 Ω), indicating a successful outcome. When we increase the repeat number of growing MnO_2 onto Co_3O_4@PPy, the R_{ct} value is enlarged (Figure 5C and the data are shown in Table S7 in ESI). The largest value (11.55 Ω) is smaller than the Co_3O_4@MnO_2, showing the effectiveness of the PPy layer.

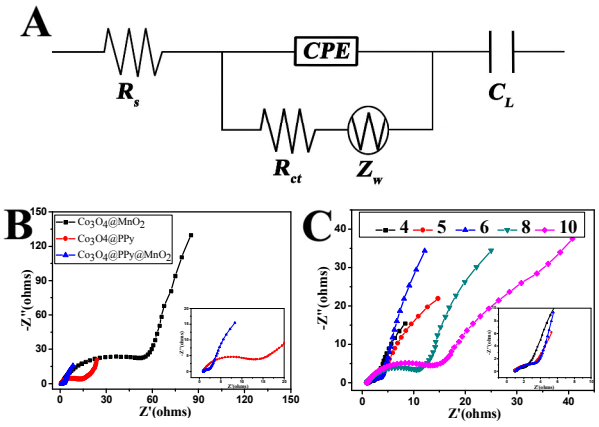

Figure 5. (A) The electrical equivalent circuit. (B) Compared EIS curves for Co_3O_4@PPy, Co_3O_4@MnO_2 and Co_3O_4@PPy@MnO_2. (C) The EIS curves for MnO_2 growth onto Co_3O_4@PPy nanowire with different repeat number.

The above analysis shows that because of the high conductivity of PPy as the sandwich layer, the electrochemical performance of Co_3O_4@PPy@MnO_2 ternary core-shell structured composite is superior to the binary core-shell structured composites. The reasons are as follows: 1) Inheriting the core-shell structure's active role in decreasing R_{ct}. The unique 3D hierarchical core-shell heterostructure has larger specific area and is beneficial to ionic diffusion of the electrolyte. 2) Taking advantage of the high conductivity of PPy to further reduce R_{ct}. Poor conductivity is a common failing of the metal oxide compared with the carbon material. The sandwiched PPy layer serves as a transition (the electrochemical performance of itself cannot be ignored), and the charge transfer will become more effective. So the pesudocapacitor behaviors of MnO_2 and Co_3O_4 are optimized. As a result, the R_{ct} of the whole course is reduced. 3) Providing a larger real reaction area. Compared with pure Co_3O_4 nanowires, the surface area of the nanowires after coating the PPy layer is enlarged (because the diameter of the nanowires is increased). In addition, different structures of MnO_2 on different nanowires also play a role on the electrochemical performance (Figures 1 and 2). Compared with nanoparticles (Figure S2 A in ESI), the MnO_2 nanosheet structure on Co_3O_4@PPy provides more favorable reaction conditions.

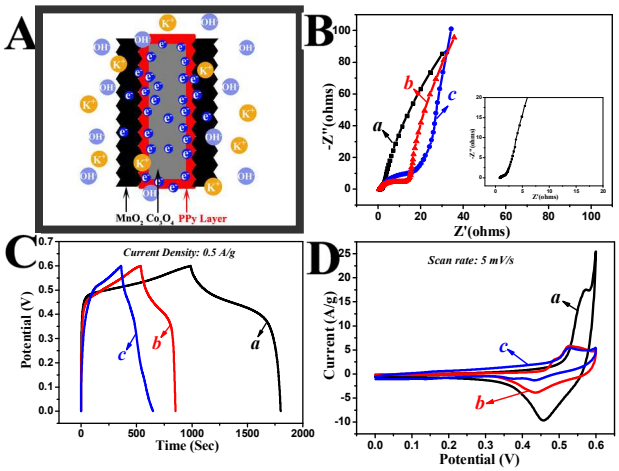

Figure 6. (A) The schematics for the optimization function by the intervened high conductive layer. Compared EIS (B), CD (C) and CV (D) curves for Co_3O_4@PANI@NiOOH (curve a), Co_3O_4@PANI (curve b), Co_3O_4@NiOOH (curve c).

To further verify the effect of the interpolation layer on decrease of R_{ct}, Co_3O_4@PANI@NiOOH ternary core-shell structured composite is tested (the SEM and TEM images are shown in Figure S1-2 in ESI). The R_{ct} of Co_3O_4@PANI@NiOOH is 0.6 Ω, which is much smaller than Co_3O_4@PANI (13.1 Ω) and Co_3O_4@NiOOH (20.6 Ω, Figure 6B and Table S10 in ESI). The electrochemical performance of the ternary core-shell composite is the best: the highest current response (Figure 6C) and a longest discharge time (Figure 6D). The specific capacitance of Co_3O_4@PANI@NiOOH (673 F/g) is 2.5 times larger than Co_3O_4@NiOOH (256 F/g) Co_3O_4@PANI (253 F/g). Furthermore, the R_{ct} of Co_3O_4@PPy@NiOOH and Co_3O_4@PPy@MnO_2 are both reduced compared with the corresponding binary core-shell composites (Figure S8 and S9 in ESI). The four groups of data demonstrate that our method (by incorporating high conductive material) reduces R_{ct}.

Conclusions

In summary, high conductive PPy or PANI layer is incorporated into the binary core-shell composite to reduce charge transfer resistance and improve electrochemical performance. The charge transfer process of the four ternary core-shell structured composites (Co_3O_4@PPy@MnO_2, Co_3O_4@PANI@NiOOH, Co_3O_4@PPy@NiOOH, Co_3O_4@PANI@MnO_2) are greatly improved, with the performances better than binary core-shell composites. These positive results indicate that our design has potential in the construction of the next generation of

supercapacitors with high performance.

Acknowledgments

This work was supported by National Natural Science Foundation of China (21353003), Special Innovation Talents of Harbin Science and Technology (2013RFQXJ145), Fundamental Research Funds of the Central University (HEUCFZ), Natural Science Foundation of Heilongjiang Province (B201316), Program of International S&T Cooperation special project (2013DFA50480), the fund for Transformation of Scientific and Technological Achievements of Harbin (2013DB4BG011).

Electronic Supplementary Information (ESI)

Electronic Supplementary Information is available from the Internet or from the author.

Notes and references

[a] *Key Laboratory of Superlight Material and Surface Technology, Ministry of Education, Harbin Engineering University, 150001, P. R. China.*

[b] *State Key Laboratory of Polymer Physics and Chemistry, Changchun, Institute of Applied Chemistry, Chinese Academy of Sciences, Changchun 130022, China.*

[c] *Institute of Advanced Marine Materials, Harbin Engineering University, 150001, P. R. China.*

** Corresponding author: Tel: +86 451 8253 3026; Fax: +86 451 8253 3026. E-mail address: zhqw1888@sohu.com†, qiliu@hrbeu.edu.cn†.*

[1] J.P. Holdren, *Science* 2007, 315, 737.

[2] G.H. Yu, X. Xie, L.J. Pan, Z.N. Bao and Y.Cui, *Nano Energy* 2013, **2**, 213-234.

[3] E. Frackowiak, S. Delpeux, K. Jurewicz, K. Szostak, D. Cazorla-Amoros and F. Beguin, *Chem. Phys. Lett.* 2002, **361**, 35-41.

[4] Y. Sui, J. Appenzeller, *Nano Lett.* 2009, **9**, 2973–2977.

[5] C. Peng, S. W. Zhang and D. Jewell, Prog. *Nat. Sci.* 2008, **18**, 777-788.

[6] C. Wei, M.L. Chang, C. Peng, C.Q. Sun, *Electrochim. Acta* 2007, **52**, 2845-2849.

[7] Y. R. Ahn, M.Y. Song, S.M. Jo and C. R. Park, *Nanotechnology* 2006, **17**, 2865.

[8] J.P. Liu, J. Jiang, C.W. Cheng, H.X. Li, J.X. Zhang, H. Gong and H.J. Fan, *Adv. Mater.* 2011, **23**, 2076-2081.

[9] L.H. Bao, J.F. Zang and X.D. Li, Nano Lett. 2011, **11**, 1215-1220.

[10] D.T. Dam and J.M. Lee, *Nano Energy* 2013, **2**, 933-942.

[11] Z. Tang, C.H. Tang and H. Gong, *Adv. Funct. Mater.* 2012, **22**, 1272-1278.

[12] J. Jiang, Y.Y. Li, J.P. Liu, X.T. Huang, C.Z. Yuan and X.W. Lou, *Adv. Mater.* 2012, **24**, 5166.

[13] V. Sridhar, H.J. Kim, J.H. Jung, C.G. Lee,S.J. Park and I.K. Oh, *ACS Nano* 2012, **6**, 10562-10570.

[14] D.H. Lee, J.E. Kim, T.H. Han, J.W. Hwang, S. Jeon, S.Y. Choi, S.H. Hong, W.J. Lee, R.S. Ruoff and S.O. Kim, *Adv. Mater.* 2010, **22**, 1247-1252.

[15] B. Wang, Q. Liu, J. Han, X.F. Zhang, J. Wang, Z.S. Li, H.J. Yan and L.H. Liu, *J. Mater. Chem. A* 2014, **2**, 1137-1143.

[16] J.P. Liu, J. Jiang, M. Bosman and H.J. Fan, *J. Mater. Chem.* 2012, **2**, 2419-2426.

[17] F. Yang, J.Y. Yao, F.L. Liu, H.C. He, M. Zhou, P. Xiao and Y.H. Zhang, *J. Mater. Chem.* A 2013, **1**, 594-601.

[18] L.Q. Mai, F. Dong, X. Xu, Y.Z. Lou, Q.Y. An, Y.L. Zhao, J. Pan and J.N. Yang, *Nano Lett.* 2013, **13**, 740-745.

[19] J.Y. Liao, D. Higgins, G. Lui, V. Chabot, X.C. Xiao and Z.W. Chen, *Nano Lett.* 2013, **13**, 5467-5473.

[20] Q. Li, Z.L. Wang, G.R. Li, R.Guo, L.X. Ding and Y.X. Tong, *Nano Lett.* 2012, **12**, 3803-3807.

[21] J.W. Liu, J. Essner and J. Li, *Chem. Mater.* 2010, **22**, 5022-5030.

[22] X.H. Xia, J.P. Tu, Y.Q. Zhang, X.L. Wang, C.D. Gu, X.B. Zhao and H.J. Fan, *ACS Nano* 2012, **6**, 5531-5538.

[23] X.H. Lu, T. Zhai, X.H. Zhang, Y.Q. Shen, L.Y. Yuan, B. Hu, L. Gong, J. Chen, Y.H. Gao, J. Zhou, Y.X. Tong and Z.L. Wang, *Adv. Mater.* 2012, **24**, 938-944.

[24] L. Yu, G.Q. Zhang, C.Z. Yuan and X.W. Lou, *Chem. Commun.* 2013, **49**, 137-139.

[25] W. Tian, X. Wang, C.Y. Zhi, T.Y. Zhai, D.Q. Liu, C. Zhang, D. Golberg, and Y. Bando, *Nano Energy* 2013, **2**, 754-763.

[26] L. Huang, D.C. Chen, Y. Ding, S. Feng, Z.L. Wang and M.L. Liu, *Nano, Lett.* 2013, **13**, 3135-3139.

[27] C.H. Tang, X.S. Yin and H. Gong, *ACS Appl. Mater. Interfaces* 2013, **5**, 10574-10582.

[28] G.F. Cai, J.P. Tu, D. Zhou, J.H. Zhang, Q.Q. Xiong, X.Y. Zhao, X.L. Wang and C.D. Guo, *J. Phys. Chem. C* 2013, **117**, 15967-15975.

[29] C. Zhou, Y.W. Zhang, Y.Y. Li and J.P. Liu, *Nano Lett.* 2013, **13**, 2078-2085.

[30] H.J. Zheng, J.X. Wang, Y. Jia and C.A. Ma, *J. Power Sources* 2012, **216**, 508-514.

[31] Y. Xia, Z. Xiao, X. Dou, H. Huang, X.H. Lu, RJ. Yan, Y.P. Gan, W.J. Zhu, J.P. Tu, W.K. Zhang and X.Y. Tao, *ACS Nano* 2013, **7**, 7083-7092.

[32] X.Y. Wang, X.Y. Wang. L.H. Yi, L. Liu, Y.Z. Dai and H. Wu. *J. Power Sources* 2013, **224**, 317-323.

[33] J.G. Wang, Y. Yang, Z.H. Huang and F.Y. Kang, *Electrochim. Acta* 2012, **75**, 213-219.

[34] D.T. Dam and J.M. Lee, *Nano Energy* 2013, **2**, 1186-1196.

[35] D.T. Dam, X. Wang and J.M. Lee, *Nano Energy* 2013, **2**, 1303-1313.

[36] C. Guan, X.H. Xia, N. Meng, Z.Y. Zeng, X.H. Cao, C. Soci, H. Zhang and H.J. Fan, *Energy Environ. Sci.* 2012, **5**, 9085-9090.

[37] L. Yu, G.Q. Zhang, C.Z. Yuan and X.W. Lou, *Chem. Commun.* 2013, **49**, 137-139.

[38] J. Ge, H.B. Bai, W. Hu, X.F. Yu, Y.X. Yan, L.B. Mao, H.H. Li, S.S. Li, S.H. Yu, *Nano Energy* 2013, **2**, 505-513.

[39] W. Yao, H. Zhou and Y. Lu, *J. Power Source* 2013, **241**, 359-366.

[40] J. Li, L. Cui and X.G. Zhang, *Appl. Surf. Sci.* 2010, **256**, 4339-4343.

[41] J.G. Wang, Y. Yang, Z.H. Huang and F.Y. Kang, *J. Mater. Chem.* 2012, **22**, 16943-19649.

[42] W. Yao, H. Zhou and Y. Lu, *J. Power Sources* 2014, **241**, 359-366.

[43] P. Li, Y. Yang, E. Shi, Q. Shen, Y. Shang, S. Wu, A.Y. Cao and D.H. Wu, *ACS Appl. Mater. Interfaces* 2014, **6**, 5228-5234.

[44] R. Tummala, R.K. Guduru and P.S. Mohanty, *J. Power Source* 2012, **209**, 44-51.

[45] M.J. Zhi, A. Manivannan, F.K. Meng, N.Q. Wu, *J. Power Source* 2012, **208**, 345-353.

[46] P.H. Yang, X. Xiao, Y.Z. Li, Y. Dong, P.F. Qiang, X.H. Tan, W.J. Mai, Z.Y. Lin, W.Z. Wu, T.Q. Li, H.Y. Jin, and Z.L. Wang, *ACS Nano* 2013, **7**, 2617-2626.

[47] X. Lu, M. Yu, G. Wang, T. Zhai, S. Xie, Y. Ling, Y. Tong and Y. Li, *Adv. Mater.* 2013, **25**, 267-272.

[48] S. Dong, X. Chen, L. Gu, X. Zhou, L. Li, Z. Liu, P. Han, H. Xu, J. Yao, H. Wang, X. Zhang, C. Shang, G. Cui and L.Chen, *Energy Environ. Sci.* 2011, **4**, 3502-3508.

[49] R. Liu, J. Duay and S.B. Lee, ACS Nano 2010, **4**, 4299-4307.

[50] J. Yan, E. Khoo, A. Sumboja and P.S. Lee, *ACS Nano* 2010, **4**, 4247-4255.